PCCP

ROYAL SOCIETY OF CHEMISTRY

PAPER

View Article Online
View Journal | View Issue

Cite this: *Phys. Chem. Chem. Phys.*, 2025, **27**, 20063

High-temperature phase evolution in CuO/Al_2O_3 oxygen carriers: insights from *in situ* quick XAS

Sharmin Sharna, *[abc] Virgile Rouchon,*[b] Arnold Lambert,[b] Valerie Briois,[c] David Chiche,[b] Anne-Sophie Gay,[b] Christèle Legens[b] and Ovidiu Ersen[a]

Received 26th January 2025,
Accepted 26th August 2025

DOI: 10.1039/d5cp00358j

rsc.li/pccp

This study investigates phase transitions in CuO/Al_2O_3 oxygen carriers during chemical looping combustion (CLC), aiming to understand performance and stability over extended redox cycles. *In situ* quick X-ray assorption spectroscopy (QXAS) was employed to track the transformations of the copper aluminate phase ($Cu_xAl_yO_4$) over 50 redox cycles in various oxidizing (2.5 to 21% O_2 in N_2) and reducing (H_2, CO, CH_4) environments. The study reveals that the oxygen carrier undergoes significant phase transitions, reaching a threshold where $Cu_xAl_yO_4$ predominantly converts to copper oxide and α-Al_2O_3, leading to irreversible structural modifications. Complementary SEM analysis further highlights morphological changes, such as particle growth prior to α-Al_2O_3 formation. This cycle-dependent phase evolution provides new insights into accelerated ageing mechanism involving the interplay between copper phase transformations and α-Al_2O_3 formation, which is critical for enhancing the durability of oxygen carriers in CLC applications.

Introduction

The escalating levels of atmospheric CO_2 and their impact on global climate underscore the urgent need for effective emission reduction strategies.[1] Implementing renewable energy sources and CO_2 capture technologies is paramount in this effort. Chemical looping combustion (CLC) process presents a promising approach for utilizing fossil fuels while inherently capturing CO_2.[2] CLC divides fuel combustion into distinct reduction and oxidation steps, enabled by a metal-oxide-based oxygen carrier (OC). In the "fuel reactor," the OC undergoes reduction by the fuel, yielding the formation of CO_2 and H_2O, which are readily separable. The subsequent re-oxidation of the reduced OC in the "air reactor" completes the redox cycle, typically conducted at temperatures exceeding 800 °C. This sequential process effectively isolates CO_2 from N_2 and O_2, eliminating the need for an energy-intensive post-combustion separation step.[3]

To achieve economic viability, the development of efficient oxygen carrier materials is crucial.[4] Among these, supported copper-based OCs, particularly CuO/Al_2O_3, are promising due to their cost-effectiveness, environmental compatibility, and versatile redox properties, making them suitable for industrial applications.[5] However, these materials exhibit challenges such as degradation and reduced reactivity at temperatures above 900 °C.[6,7] Mechanisms such as attrition, fragmentation, and sintering of copper oxides contribute to these issues, exacerbated by the phase transformations of CuO and Al_2O_3 during the redox cycles.[6,8,9]

Recent studies, including findings by Cabello *et al.*, underline the sensitivity of OC performance to temperature variations during redox cycling.[9] At elevated temperatures, solid-state reactions between CuO and Al_2O_3 lead to the formation of $CuAl_2O_4$. Initially comprising $CuAl_2O_4$, gamma alumina, and traces of CuO phases, the OC evolves after prolonged cycling at 800 °C, transforming predominantly into CuO and alpha alumina.[9] The kinetics and extent of α-alumina formation are influenced by factors such as temperature and cycle number, as we previously elucidated using advanced spectroscopic and microscopic techniques (SEM, STEM, STXM).[10] In our previous work (ChemCatChem, 2023),[10] we investigated these degradation mechanisms using post-mortem STXM-XANES and STEM-EDS after 50 and 200 redox cycles. We proposed a mechanistic framework involving: (i) competition between CuO and $Cu_xAl_yO_4$ formation depending on alumina polymorph and temperature, (ii) CuO particle growth during cycling, and (iii) the γ-to-α-Al_2O_3 phase transition driven by copper presence and heat. These changes result in copper segregation, porosity increase, and ultimately reduced oxygen carrier performance. However, this prior study was inherently limited to static snapshots and could not resolve the dynamics or sequence of transformations during redox cycling.[10]

[a] *Institut de Physique et de Chimie des Matériaux de Strasbourg, 67034 Strasbourg, France. E-mail: s.sharna@outlook.com*
[b] *IFP Energies nouvelles, Rond-point de l'échangeur de Solaize, BP 3, 69360 Solaize, France. E-mail: virgile.rouchon@ifpen.fr*
[c] *Synchrotron Soleil, l'Orme des Merisiers, BP48 Saint-Aubin, 91192 Gif-sur-Yvette, France*

Despite recent advancements, critical aspects of phase transition dynamics during redox cycling remain unresolved. In particular, the identification of transient intermediate species, the kinetics and mechanism of α-Al_2O_3 formation, and the interplay between copper phase transformation and support evolution are not fully understood. These complexities significantly influence the long-term reactivity, stability, and structural integrity of CuO/Al_2O_3 oxygen carriers. Since industrial CLC processes involve cycle times of several hours, studying degradation phenomena under practical constraints requires accelerated aging strategies to replicate long-term behavior within a feasible experimental timeframe.

To address these questions, we employed *in situ* quick X-ray absorption spectroscopy (QXAS) to provide sub-second temporal descriptions of chemical species, essential for monitoring intermediate species in fast-kinetic reactions. Although XAS is commonly applied in catalytic studies,[11,12] its use in chemical looping reactions remains relatively unexplored,[13] offering a unique opportunity to monitor intermediate species and degradation pathways under realistic conditions. To replicate long-term behavior within a feasible experimental timeframe, we applied accelerated cycling ($\sim$6 minutes per cycle)—significantly shorter than industrial CLC cycles—to induce early-stage aging effects. Post-mortem SEM was used to correlate chemical transformations with morphological evolution.

We further investigated the effects of O_2 concentration (2.5–21%) and different reducing gases (H_2, CO, CH_4) to probe how redox conditions influence phase transitions—critical for both classical CLC and CLOU (Chemical Looping with Oxygen Uncoupling), where oxygen is released directly from the OC.

This work significantly extends our prior study by revealing that Cu-aluminate breakdown follows a nucleation and growth mechanism and that the γ-to-α-Al_2O_3 transition is both temperature- and copper-dependent. By compressing 50 cycles into a short experimental timeframe, we simulate long-term aging and capture dynamic transformations that directly inform oxygen carrier design for industrial CLC systems.

Materials and methods

Material synthesis: impregnation

A CuO/Al_2O_3 oxygen carrier containing 13 wt% CuO was prepared by incipient wetness impregnation. A total of 9.1 g of copper(II) nitrate trihydrate ($Cu(NO_3)_2{\cdot}3H_2O$, Sigma-Aldrich, $\geq$99%) was dissolved in 10 mL of deionized water, corresponding to the total pore volume of 20 g of γ-Al_2O_3 (Puralox SCFa-140, Sasol; pore volume = 0.5 mL g^{-1}, surface area = 140 m^2 g^{-1}).

The impregnation was carried out using a custom-built setup consisting of a shallow, tilted glass vessel rotated by a motor to ensure uniform distribution of the precursor solution. The vessel was positioned at a 45° angle and rotated at approximately 20 rpm. The copper nitrate solution was added dropwise to the alumina support while manually stirred using a spatula. The setup included a rotary evaporator bezel placed on a rotating platform to maintain uniform mixing throughout the impregnation.

After impregnation, the sample was aged for 3 hours in a sealed, desiccator-like glass chamber containing a water reservoir, which created a high-humidity atmosphere (estimated relative humidity >75%, not quantitatively controlled).

The impregnated material was then dried overnight at 120 °C using a 5 °C min^{-1} ramp, followed by calcination in static air at 900 °C for 12 hours with the same ramp rate. The detailed characterization of the fresh sample has been published elsewhere.[10]

Reference samples

CuO, Cu_2O, $CuAl_2O_4$, $CuAlO_2$, and metallic copper, along with non-stoichiometric phases such as $Cu_xAl_yO_4$ and $Cu_xAl_yO_2$, were identified and used as reference phases. Their crystal structures are shown as ball-and-stick models in Section S1.

The commercial powders of CuO and Cu_2O from Sigma Aldrich were used as reference standards.

A bulk $CuAl_2O_4$ spinel phase was synthesized by solid-state reaction. Copper(II) oxide (CuO, Sigma-Aldrich, $\geq$99%) and γ-Al_2O_3 (Puralox SCFa series, Sasol) were combined in a 1 : 1 molar ratio and thoroughly mixed using manual grinding in an agate mortar for 15 minutes to ensure homogeneity. The resulting powder was calcined in air at 600 °C for 12 hours (heating ramp: 5 °C min^{-1}) to initiate spinel phase formation while preventing the transition of γ-Al_2O_3 to α-Al_2O_3. The grinding and calcination steps were repeated a second time under the same conditions to promote reaction completion and structural uniformity. Finally, the material underwent a high-temperature calcination at 900 °C for 12 hours (ramp: 5 °C min^{-1}) to stabilize the $CuAl_2O_4$ phase. The resulting powder was used as a bulk reference sample for structural and spectroscopic comparisons. No ball milling or mechanochemical synthesis was employed in this procedure. The XRD pattern is shown in Fig. S2 and includes a minor impurity phase of α-Al_2O_3.

For the non-stoichiometric copper aluminate spinel phase, the fresh 13 wt% CuO/Al_2O_3-900 sample (before redox reactions) was used as a reference. This corresponds to a formula $Cu_{0.24}Al_{2.51}O_4$, referred to as $Cu_xAl_yO_4$ in the manuscript.

The delafossite $CuAlO_2$ sample was synthesized by calcining stoichiometric $CuAl_2O_4$ at 950 °C under an inert N_2 atmosphere for 10 hours. Similarly, non-stoichiometric $Cu_xAl_yO_2$ was prepared by calcining the 13 wt% CuO/Al_2O_3-900 sample at 950 °C under an inert N_2 atmosphere for 10 hours. The synthesis protocol was adapted considering the phase diagram of the Cu–Al–O system.[14] T Although XRD data for the $CuAlO_2$ phase could not be obtained, characteristic spectral features and comparison with literature strongly support the presence of the delafossite $CuAlO_2$ phase. While the presence of minor impurities such as $CuAl_2O_4$ or Al_2O_3 cannot be entirely excluded, their contributions are likely minimal and do not materially impact the interpretation of the spectroscopic data.

Material ageing

The post-mortem samples characterized using SEM were aged in a thermogravimetric analyzer (Setaram TAG 24). The reaction and aging of the materials were conducted through redox cycles, alternating between reducing (10% H_2, 90% N_2) and oxidizing (air) gases for 1.5 minutes each. To prevent the mixing of H_2 and air, the TGA system was purged with N_2 gas for 1.5 minutes between the reduction and oxidation steps at 900 °C. The gas flow rate was maintained at 150 mL min^{-1}.

Characterization techniques

SEM. SEM imaging with semi-quantitative elemental analysis was performed using an FEI Nova nanoSEM 450 equipped with an Oxford XMAX 80 EDS detector operating at 15 keV. The polished cross-section samples were prepared by embedding the OC grains in epoxy resin and polishing them with a SiC sheet.

For the SEM, fresh OC, post-mortem samples after 1, 5, 10, 20 and 50 cycles were characterized. Similarly, the sample from *in situ* XAS experiment was also collected and characterized in SEM, the sample preparation was similarly carried out by embedding in epoxy resin.

***In situ* XAS.** The Quick XAS experiments were conducted at the ROCK beamline at the SOLEIL synchrotron. Data acquisition was performed at the Cu K-edge (8980–8990 eV) in transmission mode using two nitrogen-filled ionization chambers. Fast *in situ* data acquisition of the copper catalysts was achieved using a quick-XAS monochromator equipped with a Si (111) channel-cut crystal, set to acquire spectra with an acquisition time of 0.25 s per spectrum. The powdered sample was loaded into a dedicated sample environment placed between two Oken ionization chambers filled with nitrogen for detecting incident and transmitted X-rays. Energy calibration was ensured by simultaneously measuring the absorption spectrum of a Cu metallic foil placed between the second and third ionization chambers. The cell allowed for *in situ* treatments of the sample under controlled conditions of temperature and gas flow throughout the experiment.

The temperature was increased from room temperature to 500 °C at a rate of 20 °C min^{-1}, then at 15 °C min^{-1} from 500 °C to 700 °C, and at 10 °C min^{-1} from 700 °C to 900 °C. This stepwise heating was implemented to ensure the thermal stability of the furnace. After reaching the target temperature, oxidation and reduction reactions were performed using the respective gases, with N_2 gas purging in between each reaction.

Three experiments were designed to investigate the effects of different reducing gases (H_2, CO, and CH_4) under a fixed oxygen partial pressure of 2.5%, while a fourth experiment assessed the impact of varying oxygen partial pressure using air (21% O_2) for oxidation. The details of these four experiments are summarized in Table S2 which includes parameters such as flow rates, sample mass, and reaction durations. The samples were named based on the gases used during the reactions; for example, the sample labeled H_2–O_2 was reduced with 2.5% H_2/N_2 and oxidized with 2.5% O_2/N_2.

As a precautionary note, we acknowledge potential concerns regarding the completeness of the reaction, particularly under conditions of low oxygen partial pressure and the associated gas diffusion limitations within the reactor, especially in the H_2–air dataset. The low O_2 partial pressures during the oxidation steps of the H_2–O_2, CO–O_2, and CH_4–O_2 experiments likely resulted in incomplete oxidation in certain regions, contributing to the gradual accumulation of copper/copper oxide phases through sintering.

However, it is important to clarify that the observed main phenomenon were consistently observed across both *in situ* and *ex situ* experiments.

The QXAS raw data were calibrated and normalized using the normal_gui Python interface developed at SOLEIL.[15] Subsequently, the normalized $\mu(E)$ QXAS spectra underwent data analysis using multivariate curve resolution with alternating least squares (MCR-ALS), a chemometrics technique well-suited for handling large datasets. The MCR-ALS minimization process was performed using MATLAB's MCR-ALS GUI 2.0, developed by Jaumot *et al.*[16] Comprehensive methodologies for applying MCR-ALS to XAS spectra can be found in the existing literature,[17,18] and further details specific to this study are provided in Section S3.

The pure species spectra extracted *via* MCR-ALS were validated against reference spectra (Fig. S6–S10), as high-temperature data often deviate from room temperature profiles due to thermal effects such as the Debye–Waller factor. This comparison, detailed in Section S4, was essential for accurate component identification. While Fourier transforms (FT) of the EXAFS data are included in Fig. S6–S10, they were not used in the fitting due to strong thermal disorder at 900 °C. Elevated temperatures significantly increase the Debye–Waller factor, resulting in damping of EXAFS oscillations—particularly at high *k*-values. Consequently, even first-shell Cu–O peaks exhibit reduced amplitude, while second-shell Cu–Cu and Cu–Al contributions are often absent or poorly resolved. This is clearly reflected in the FTs, where only broad or partial first-shell signals are visible and higher-shell features are largely suppressed.

The post-mortem and *ex situ* reference measurements were performed on pressed pellets; each XAS pellet contained approximately 10 wt% of the copper-containing sample diluted with boron nitride (BN), a proportion chosen to ensure reliable transmission at the Cu K-edge.

Results and discussions

The first section presents a detailed analysis of the 2.5% H_2–2.5% O_2 dataset, examining reactions at each step. Subsequently, the effects of different reducing gases and oxygen partial pressures are discussed, alongside the morphological analysis of postmortem and aged samples.

Evolution of chemical species under H_2 and O_2

Heating from 25 °C to 900 °C under 2.5% O_2. Fig. 1 (left) shows spectral changes during heating from 20 °C to 900 °C under 2.5% O_2. Initially, the sample is composed mainly of

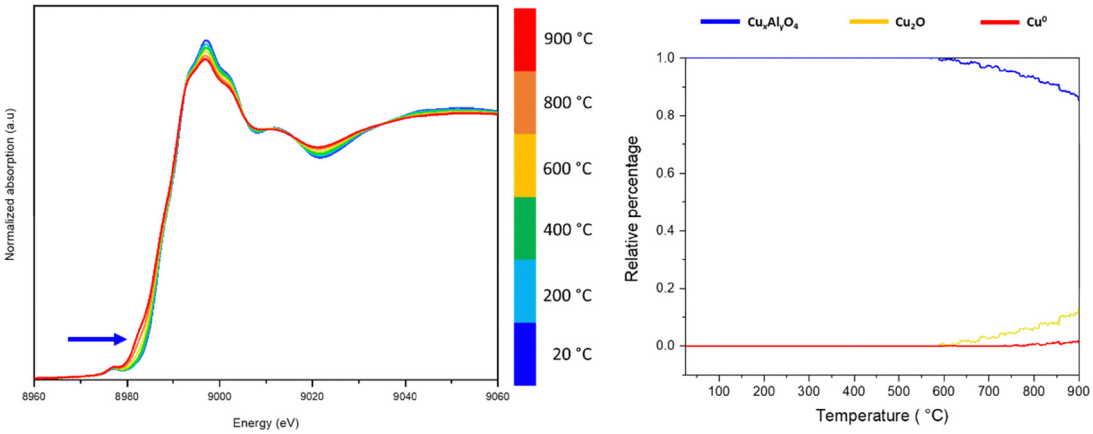

Fig. 1 Spectral evolution during ramp up for H_2–O_2 (left) and the corresponding concentration profile of the $CuAl_xO_y$, Cu_2O and Cu^0 as a function of the temperature ramp under 2.5% O_2.

$Cu_xAl_yO_4$. As the temperature rises, the main peak at 8996 eV decreases, with additional damping in the multiple scattering zone and slight peak broadening near the 8977 eV pre-edge feature. Around 600 °C, a bump-like feature appears at approximately 8982 eV, corresponding to Cu^{1+}. Fig. 1 (right) illustrates the composition changes due to heating. By 900 °C heating, the composition consists of about 85% $Cu_xAl_yO_4$ and 15% Cu_2O. This evolution could be attributed to the stability of copper-alumina phases, which varies with oxygen partial pressure and temperature.[14] $CuAl_2O_4$ can decompose into Cu_2O and alumina, while other studies have also reported the formation of the Cu_2O phase under similar conditions.[19]

Oxidation–reduction cycles

After heating under 2.5% O_2, the sample underwent 50 reduction–oxidation cycles, with an inert gas step in between. Fig. 2 shows the spectral changes every 10 cycles. Approximately 2000 spectra were generated to capture minute gas-induced changes, though intermediate spectra are omitted for clarity.

Initially, the oxidized phase resembles the reference spectra of $Cu_xAl_yO_4$, with a distinct pre-edge peak around 8978 eV. The reduced phase resembles metallic copper foil, with less pronounced features due to nanoparticle formation during copper aluminate reduction. Over cycles, spectral changes appear in both oxidized and reduced states. In the oxidized sample, a bump near 8983 eV emerges (Cu_2O), while the $Cu_xAl_yO_4$ pre-edge diminishes. In the reduced state, metallic copper spectra become more subdued with cycling. On the right shows the spectral evolution and concentration profile of different species for the 1st cycle, highlighting the shift from oxidized to reduced states. The shift in spectral features, marked with arrows, demonstrates the evolution in oxidation state from the oxidized state (blue line) to the reduced state (red line) during reduction.

Evolution of the species as a function of the reaction gases

Fig. 3 presents the spectral contributions of different species extracted *via* MCR-ALS analysis. A description of the methodology, comparison with reference phases at room temperature, and corresponding XAS characterization are provided in S4 (Fig. S6–S10). The left panel of Fig. 3 shows the concentration profiles of these species during the first cycle, also obtained from MCR-ALS. The possible reactions occurring under N_2, H_2, and O_2 environments are summarized in Table 1.

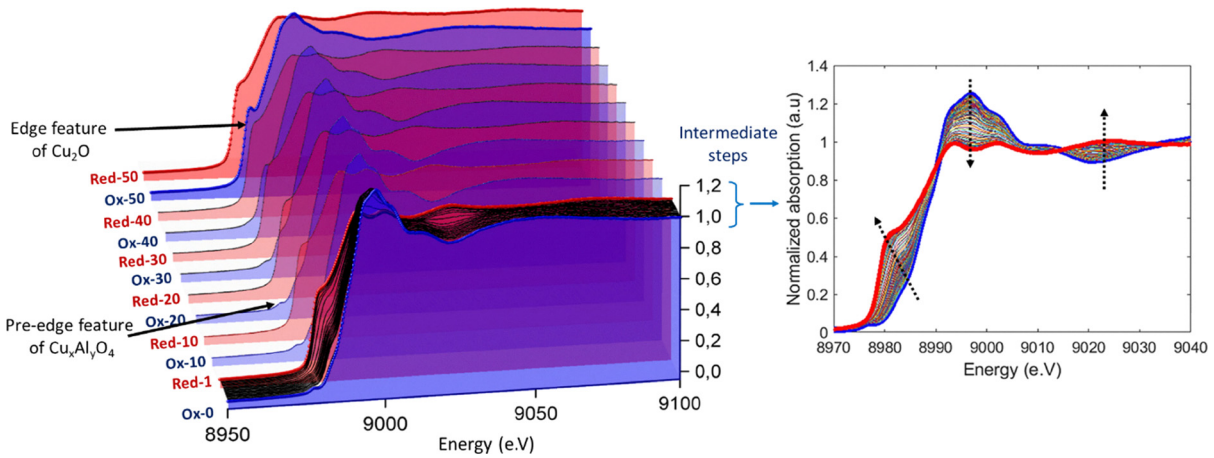

Fig. 2 Spectral change over 50 redox cycles represented for every 10 cycles for the 2.5% H_2–2.5% O_2 sample.

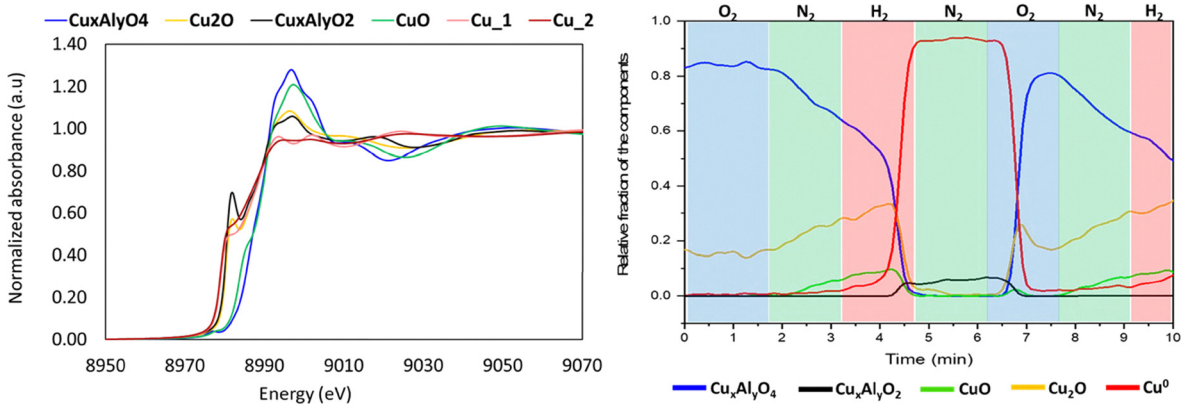

Fig. 3 Spectral contributions (left) and concentration profiles (right) of species identified by MCR-ALS under N_2, H_2, and O_2 atmospheres.

Inert gas. At the start of the 1st cycle, the sample remains under 2.5% O_2 before switching to N_2 for 90 s (Fig. 3, right, green area). During this time, $Cu_xAl_yO_4$ decreases while Cu_2O increases, likely *via* reaction (R2). No $Cu_xAl_yO_2$ is observed, in contrast to prior reports[8,14,19]—likely due to our shorter heating duration compared to the extended annealing (>1000 °C) used in those studies. CuO and trace metallic Cu appear briefly, likely from reaction (R3), but remain below 5%, requiring cautious interpretation. The final composition is ~60–65% $Cu_xAl_yO_4$, ~25–30% Cu_2O, and <5% CuO.

Reduction. Upon H_2 introduction, $Cu_xAl_yO_4$ rapidly disappears within 45 s (reactions (R4) and (R5)), while Cu_2O peaks (~35%) at 60 s and then declines. CuO follows a similar trend. Metallic Cu increases and dominates by the end of the step (>90%). $Cu_xAl_yO_2$ forms transiently (~6%), likely *via* reaction (R9) between Cu_2O and alumina released from aluminate reduction. This suggests $Cu_xAl_yO_4$ reduces through a Cu_2O intermediate, as reported for CuO.[18,20]

Inert gas. Under N_2, metallic Cu remains stable, while Cu_2O continues reducing and vanishes after ~45 s. A slight increase in $Cu_xAl_yO_2$ supports the occurrence of reaction (R9).

Re-oxidation. Under oxidation, metallic copper is rapidly oxidized, to form Cu_2O and $Cu_xAl_yO_4$ *via* reactions (R10) and (R13). Cu_2O peaks (~25–30%) at 45 s, then declines as $Cu_xAl_yO_4$ rises (reaction (R14)). CuO also appears briefly (reactions (R11) and (R12)). These intermediates suggest a stepwise oxidation pathway. Residual metallic Cu at the end may reflect incomplete conversion due to short reaction time or gas transport limitations in the reactor.

Evolution of the species as a function of the number of cycles. Fig. 4 illustrates the concentration profiles of key species over 50 redox cycles under oxidative, reductive, and inert environments. Peaks in the $Cu_xAl_yO_4$ (blue) and Cu_2O (yellow) signals mark oxidation maxima, while metallic copper (red) corresponds to peak reduction.

To examine oxidation trends, we focus on $Cu_xAl_yO_4$, Cu_2O, and metallic copper. Their compositions at the end of each oxidation step are shown in Fig. S11 (Section S5). Over successive cycles, $Cu_xAl_yO_4$ content steadily decreases, while Cu_2O and metallic copper increase. This behavior divides naturally into two phases: cycles 1–26 (0–150 min) and 27–50 (150–300 min). Initially, $Cu_xAl_yO_4$ declines slowly (~0.3% per cycle), with a modest increase in Cu_2O. After cycle 26, the rate of $Cu_xAl_yO_4$ loss accelerates (~2.7% per cycle), while Cu_2O content increases (~2.5% per cycle), suggesting a shift in oxidation pathways.

Reduction behavior (phases at the end of each reduction cycle) is shown in Fig. S10. The dominant reduced species are metallic copper and $Cu_xAl_yO_2$, with metallic copper comprising 90–95% of the material through cycle 45 (270 min). However, during intermediate stages (cycles 18–25), $Cu_xAl_yO_2$ content transiently increases up to ~30%, coinciding with the disappearance of Cu_2O. This $Cu_xAl_yO_2$ is later reduced to metallic copper and alumina (reaction (R4)). Beyond cycle 45 (Fig. 4), $Cu_xAl_yO_2$ is nearly absent at the end of reduction, while Cu_2O increases, implying a dynamic competition between Cu_2O reduction and $Cu_xAl_yO_2$ formation—likely influenced by evolving support structure.

Table 1 Possible chemical reactions under different gas atmospheres

Inert (after oxidation)	Reduction	Oxidation
(R1) $4CuAl_2O_4 \leftrightarrow 4CuAlO_2 + 2Al_2O_3 + O_2$	(R4) $CuAl_2O_4 + H_2 \rightarrow Cu + H_2O + Al_2O_3$	(R10) $4Cu + O_2 \rightarrow 2Cu_2O$
(R2) $4CuAl_2O_4 \leftrightarrow 2Cu_2O + 4Al_2O_3 + O_2$	(R5) $2CuAl_2O_4 + H_2 \rightarrow Cu_2O + 2Al_2O_3 + H_2O$	(R11) $2Cu + O_2 \rightarrow 2CuO$
(R3) $4CuO \leftrightarrow 2Cu_2O + O_2$	(R6) $Cu_2O + H_2 \rightarrow 2Cu + H_2O$	(R12) $2Cu_2O + O_2 \rightarrow 4CuO$
	(R7) $2CuO + 2H_2 \rightarrow Cu_2O + 2H_2O$	(R13) $2Cu + O_2 + 2Al_2O_3 \rightarrow 2CuAl_2O_4$
	(R8) $CuO + H_2 \rightarrow Cu + H_2O$	(R14) $Cu_2O + 0.5O_2 + 2Al_2O_3 \rightarrow 2\ CuAl_2O_4$
	(R9) $Cu_2O + Al_2O_3 \rightarrow 2CuAlO_2$	(R15) $CuO + Al_2O_3 \rightarrow CuAl_2O_4$
		(R16) $2CuAlO_2 + 0.5O_2 \rightarrow CuAl_2O_4 + CuO$
		(R17) $2CuAlO_2 + Al_2O_3 + 0.5O_2 \rightarrow 2CuAl_2O_4$

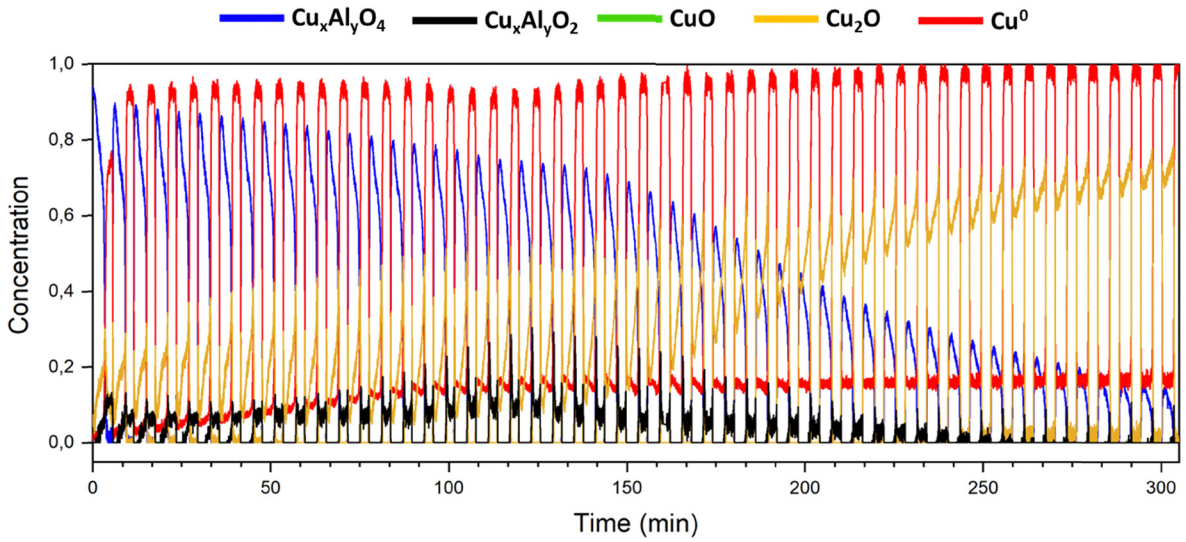

Fig. 4 Concentration profile of 2.5%H_2–2.5%O_2 gas for 50 oxidation–reduction cycles with both oxidized and reduced phases of copper containing species represented by different colors.

Although the profile shows a single metallic copper species, MCR-ALS identified two distinct spectral features: Cu0-1 and Cu0-2, representing different reduction stages. Their combined signal is reported as Cu_0 (Fig. 4 and Fig. S11–S19). Over time, Cu0-1 decreases while Cu0-2 increases, suggesting progressive changes in copper reduction behavior. As discussed in (Section S4 and Fig. S10), this shift may result from several reasons but the more plausible is due to incomplete reduction in localized regions.

Cooling from 900 °C to 25 °C

After redox cycling, the furnace temperature was gradually lowered to room temperature under 2.5% O_2. At 900 °C, the sample's composition was approximately 70% Cu_2O, 15% $Cu_xAl_yO_4$, and 15% metallic copper. As the temperature decreased, spectral changes (Fig. S13) indicated an oxidation state increase from Cu^{1+} to Cu^{2+}, evidenced by an upward shift in edge energy. Under low O_2 partial pressure, Cu_2O gradually converted to CuO *via* reaction (R3) starting at 870 °C, completing the transformation by 820 °C, in line with the Cu–O phase diagram.[21] Simultaneously, remaining metallic copper oxidized, consistent with expected oxidative conditions at lower temperatures. By the end of the cooling process, linear combination fitting (LCF) showed phase proportions of 90% CuO and 10% $Cu_xAl_yO_4$.

Effect of reducing gas

The effects of CH_4 and CO were compared with H_2 to simulate varied CLC conditions. The resulting species distributions at the end of each oxidation and reduction step are shown in Fig. S14 and S15 for CH_4, and Fig. S16 and S17 for CO, respectively.

Reduction trends. In all cases, metallic Cu dominated post-reduction (>94%), but intermediate phase behavior differed. In CH_4, $Cu_xAl_yO_2$ remained low (0–6%) and showed no consistent evolution. In contrast, H_2 and CO systems exhibited a clear rise in $Cu_xAl_yO_2$ up to ~9% around cycles 20–27, followed by a decline toward negligible levels by the end. This suggests transient Cu_2O–alumina interactions influenced by the alumina phase present.[22] Other phases ($Cu_xAl_yO_4$, Cu_2O, CuO) were largely absent, with only a brief Cu_2O signal in early CO

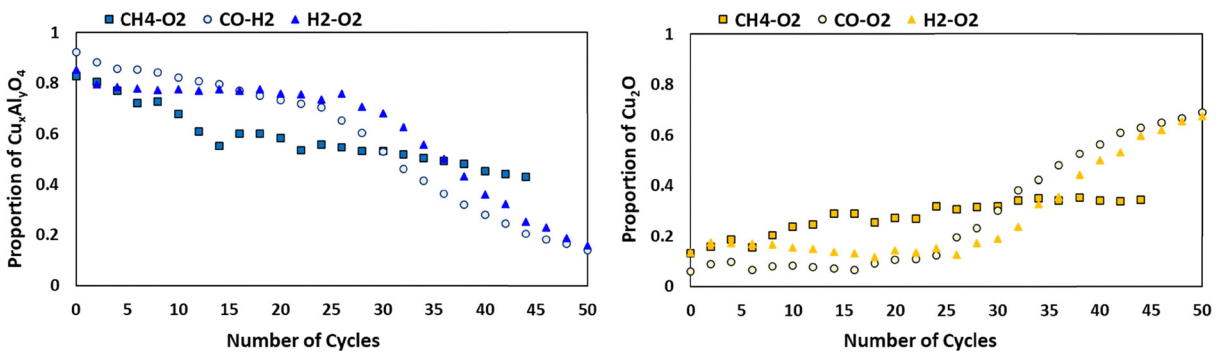

Fig. 5 The relative percentage of the $Cu_xAl_yO_4$ (left) and Cu_2O (right) at the end of the oxidation step throughout the 50 cycles for the experimental datasets CH_4–O_2, CO–O_2 and H_2–O_2.

cycles and minor end-cycle fluctuations, indicating partial reduction or kinetic limitations.

Oxidation trends. Fig. 5 presents the evolution of $Cu_xAl_yO_4$ and Cu_2O content over 50 cycles across all reducing gas environments. In all cases, oxidation led to a progressive decline in $Cu_xAl_yO_4$, accompanied by increasing amounts of Cu_2O and residual metallic Cu. However, both the rate and onset of these changes varied significantly with gas composition. In the CO–O_2 system, the $Cu_xAl_yO_4$ content decreased steadily up to cycle 24, after which a more rapid degradation occurred. This inflection point coincided with a marked increase in both Cu_2O and metallic Cu, the latter stabilizing at ~16%. In contrast, the CH_4–O_2 system exhibited a more gradual and linear decline in $Cu_xAl_yO_4$, with Cu_2O rising proportionally and metallic Cu increasing slowly but consistently.

Effect of oxygen partial pressure

The influence of O_2 partial pressure on phase evolution was assessed by comparing experiments conducted under 2.5% O_2 and atmospheric air (21% O_2). The proportions of each species at the end of the oxidation and reduction steps are provided in Fig. S18 and S19, respectively.

Oxidation trends. In the H_2–air experiment, a change in trend was observed after cycle 14, attributed to material displacement within the capillary, likely leading to reduced packing density and signal loss. To correct for this, the sample was repositioned (~80 μm) along the capillary, and only data from the second, more stable region were considered.

As seen from Fig. 6, from cycle 15 to 17, the material remained fully as $Cu_xAl_yO_4$, indicating initial phase stability. Beyond cycle 17, this phase declined steadily (~1.3% per cycle), while CuO emerged and grew to 27% by cycle 42. Cu_2O remained negligible, contrasting with its higher presence under 2.5% O_2, highlighting the effect of oxygen partial pressure on CuO/Cu_2O phase stability.

Metallic Cu stayed below 10%, with late-cycle accumulation likely reflecting incomplete oxidation in sintered regions, as supported by SEM observations.

Reduction trends. Across all experiments, metallic copper was the dominant phase after reduction (Fig. S13). In the H_2–air dataset, Cu^0 content increased steadily to ~92% by cycle 14, then stabilized around 85%. A gradual rise in Cu^0-2 features and persistent $Cu_xAl_yO_2$ toward later cycles suggest incomplete reduction compared to other conditions.

$Cu_xAl_yO_4$, Cu_2O, and CuO were largely absent during reduction, except in the first H_2–air cycle, which showed residual $Cu_xAl_yO_4$ (40%) and CuO (20%)—likely due to initial incomplete reduction. Oxygen partial pressure mainly affected which copper oxide formed: CuO appeared in H_2–air, while Cu_2O was observed in 2.5% O_2 experiments. In all cases, copper aluminate decreased gradually, followed by a sharp decline after ~20 cycles.

Morphology and correlation between copper phases and support phase transition

All datasets except CH_4–O_2 exhibited a threshold-like transition, likely linked to changes in the alumina support. To investigate, post-mortem SEM-EDS was performed on cross-sections after *in situ* XAS (Fig. 7 and Fig. S20–S23), and compared with *ex situ* TGA-cycled samples (S24). Phase identification was guided by prior spectromicroscopy work. In H_2–O_2 and CO–O_2 samples, α-Al_2O_3 grains contained embedded Cu-rich regions. Four main textures were observed: (1) low- and (2) high-Cu aluminates, (3) α-Al_2O_3, and (4) CuO. H_2–O_2 samples showed increased porosity and segregation compared to the denser aluminate observed in H_2–air. CH_4–O_2 samples differed, with α-Al_2O_3 forming at the edges and Cu-rich areas distributed throughout. A dense Cu-aluminate region was also identified—unique to this sample—possibly linked to carbon deposition inhibiting α-Al_2O_3 nucleation.[23]

Fig. S24 shows the morphological changes in samples after 0, 1, 5, 10, 20, and 50 TGA redox cycles. After ~20 cycles, patches of altered porosity and copper enrichment begin to appear, identifiable by greyscale variation. Red-highlighted regions correspond to coarse grains depleted in copper, consistent with α-Al_2O_3 formation. By 50 cycles, the material predominantly displays α-Al_2O_3 and segregated CuO, closely resembling the post-mortem H_2–O_2 and CO–O_2 samples—supporting continued phase evolution.

To investigate the microstructure, STEM-EDS analysis of regions marked in Fig. 8(a) and (b) reveals two distinct domains

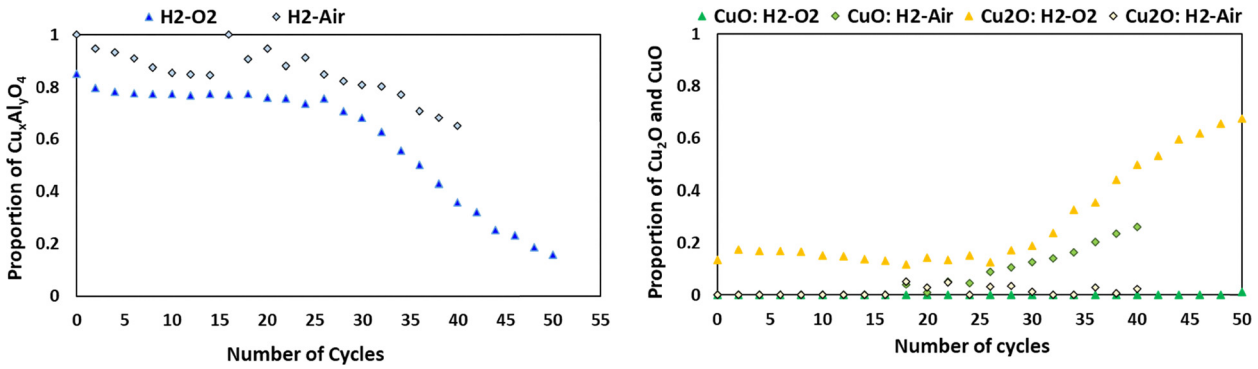

Fig. 6 Changes in the relative percentages of $Cu_xAl_yO_4$ (left) and Cu_2O–CuO phases (right) at the end of the oxidation reactions from fresh sample to up to 50 cycles for H_2–O_2 and H_2–air datasets.

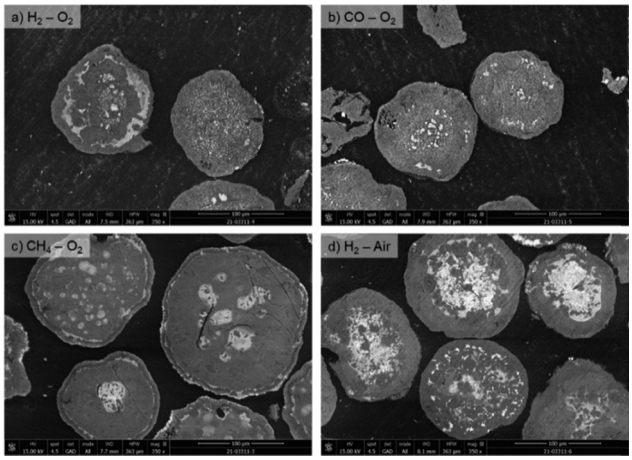

Fig. 7 SEM image of cross-cut section of (a) H_2–O_2, (b) CO–O_2, (c) CH_4–O_2 and (d) H_2–air samples.

in the 20-cycle sample: large α-Al_2O_3 grains (in red) and surrounding clusters of finer copper-aluminate particles. In the 50-cycle sample (Fig. 8(c) and (d)), the matrix is largely α-Al_2O_3 with embedded sintered CuO particles. These observations suggest that α-Al_2O_3 formation inhibits the reformation of $Cu_xAl_yO_4$, leading to irreversible CuO segregation at high temperature.[22]

This morphological evolution correlates well with the threshold behavior observed in *in situ* XAS, where a sharp decline in copper aluminate and a concurrent rise in Cu_2O were detected beyond ∼20 cycles. Together, the spectroscopic and microscopic results indicate that support transformation to α-Al_2O_3 is a key driver of irreversible copper segregation and oxygen carrier degradation.

Degradation mechanisms and structural evolution

Threshold behavior and gas environment effects. As shown in Table 2, the most rapid loss of $Cu_xAl_yO_4$ occurs in the H_2–O_2 and CO–O_2 systems, where aluminate content drops from ∼80–88% at cycle 1 to ∼28–36% at cycle 40, alongside a rise in Cu_2O. The persistence of metallic Cu after oxidation reflects both solid-state diffusional limitations during the 90 s oxidation step and progressive sintering of Cu particles.

By contrast, the H_2–air dataset shows delayed degradation, maintaining >90% $Cu_xAl_yO_4$ through cycle 20 and ∼65% by cycle 40. The higher oxygen partial pressure likely enhances Cu diffusion into alumina grains, enabling more complete reoxidation and reducing residual metallic Cu. This favors aluminate regeneration and helps preserve structural integrity.

CH_4–O_2 exhibits a more gradual transition. $Cu_xAl_yO_4$ remains at ∼45% even at cycle 40, with SEM and STEM showing a denser aluminate matrix and only peripheral α-Al_2O_3 formation. This may be attributed to carbon deposition passivating the surface or to CH_4's stronger reducibility, which favors formation of metallic Cu (Cu0_1) while suppressing Cu0_2 species—commonly linked to partially oxidized domains. The lower Cu0_2 content implies reduced sintering and enhanced copper mobility, allowing Cu to reintegrate into the support. As a result, aluminate formation is sustained and α-Al_2O_3 nucleation delayed, despite the reducing conditions.

Interestingly, both CH_4–O_2 and H_2–air—despite being redox opposites—appear to suppress sintering and promote Cu dispersion, likely *via* different mechanisms. Their shared outcome of higher copper mobility delays support degradation relative to H_2–O_2 and CO–O_2, where earlier Cu clustering and support restructuring are observed.

Role of transient Cu(I) phases. *In situ* MCR-ALS analysis reveals the transient formation of Cu(I) species—Cu_2O and $CuAlO_2$—under intermediate P_{O_2} conditions or during gas-switching transitions. $CuAlO_2$ emerges briefly during early reduction,[24] following the reaction: $CuAl_2O_4 \rightarrow CuAlO_2 \rightarrow Cu + Al_2O_3$.

The $CuAlO_2$ signal intensifies up to cycle ∼21, then fades and disappears by cycle 44. This trend reflects a kinetic intermediate that is progressively suppressed as the support evolves. Even beyond its disappearance as a major phase, brief $CuAlO_2$ spikes persist at the start of each reduction cycle, indicating that this pathway remains active until support degradation fully impedes it.

Proposed mechanism of structural evolution. Fig. 9 presents a conceptual model of the degradation mechanism based on this study and prior work (ChemCatChem, 2023).[10] During each

Fig. 8 (a), (c) STEM and (b), (d) EDS of 13 wt% CuO/Al_2O_3-900 sample cycled 20 times at 900 °C carried out in TGA, displaying Cu-aluminate/α-Al_2O_3 phases.

Table 2 Presence of $Cu_xAl_yO_4$ and copper oxide at the end of cycle 1, 20 and 40 for all the datasets

		Cycle 1 (%)	Cycle 20 (%)	Cycle 40 (%)	Key trends
H_2–O_2	$Cu_xAl_yO_4$	81	76	36	Abrupt drop in $Cu_xAl_yO_4$, Cu_2O increases sharply
	Cu_2O	14	14	50	
CO–O_2	$Cu_xAl_yO_4$	88	73	28	Similar to H_2–O_2: rapid degradation
	Cu_2O	9	11	56	
CH_4–O_2	$Cu_xAl_yO_4$	82	58	45	More gradual change, less Cu oxide overall
	Cu_2O	13	27	34	
H_2–air	$Cu_xAl_yO_4$	97	95	65	Delayed transition, but also substantial loss by cycle 40
	CuO + Cu_2O	0	4	28	

redox cycle, Cu is inserted into and extracted from the alumina lattice, forming $Cu_xAl_yO_4$ during oxidation and releasing metallic Cu during reduction. The stoichiometry of the aluminate phase depends on copper availability, support porosity, and gas-dependent diffusion kinetics.

During reduction, some copper particles sinter and grow, particularly when reoxidation is too brief to allow full migration back into the support. This leads to inhomogeneous copper distribution, with Cu-rich regions becoming embedded within the matrix. These regions were previously observed *via* STXM and SEM and are believed to act as for α-Al_2O_3 nucleation. However, sintering during reduction—especially if reoxidation is short or low O_2 partial pressure—leads to Cu-rich aluminate. These domains, previously visualized *via* STXM and SEM, likely act as "seeding zones" or nucleation sites for α-Al_2O_3. Once formed, α-Al_2O_3 is thermodynamically stable and resists further Cu re-incorporation, leading to progressive deactivation.

The $\gamma \rightarrow \alpha$-$Al_2O_3$ transformation follows a nucleation and growth mechanism. Several studies have shown that this transformation is not solely driven by particle size but also by incubation time and local structural rearrangement.[25–28] Bagwell *et al.*[26] emphasized that this transformation depends more on incubation time and local rearrangements than particle size alone. Cu insertion–deinsertion accelerates this process by lowering the transformation temperature and facilitating structural reorganization. Over time, this cycling drives coarsening of transition alumina grains and the formation of vermicular α-Al_2O_3 structures.[10]

Our results support this: Cu-enriched zones promote α-Al_2O_3 nucleation, which then propagates through coarsening of alumina grains. Plyasova *et al.* showed that Al^{3+} rearranges after Cu removal from $CuAl_2O_4$, forming an environment compatible with γ-Al_2O_3. Prolonged cycling under thermal stress then triggers irreversible transformation to α-Al_2O_3.[29,30] Once a critical size or number of α-phase nuclei is reached, redox cycling promotes their growth at the expense of porosity and $Cu_xAl_yO_4$ reactivity. This marks the final stage of degradation, where copper remains as sintered copper oxide on an inert α-Al_2O_3 matrix.

We hypothesize that the onset of α-Al_2O_3 formation is driven by a combination of structural reorganization and particle coarsening. However, the precise transformation pathway—including the involvement of metastable intermediates and grain growth dynamics—remains unresolved. Future *in situ* spectromicroscopic studies, particularly at the Al K-edge, will be essential to clarify these transitions and spatially correlate them with copper distribution and support morphology.

While this study focuses on Cu-based systems, the insights gained may extend more broadly to other oxygen carriers. For example, Fe-, Mn-, and Co-based materials also experience

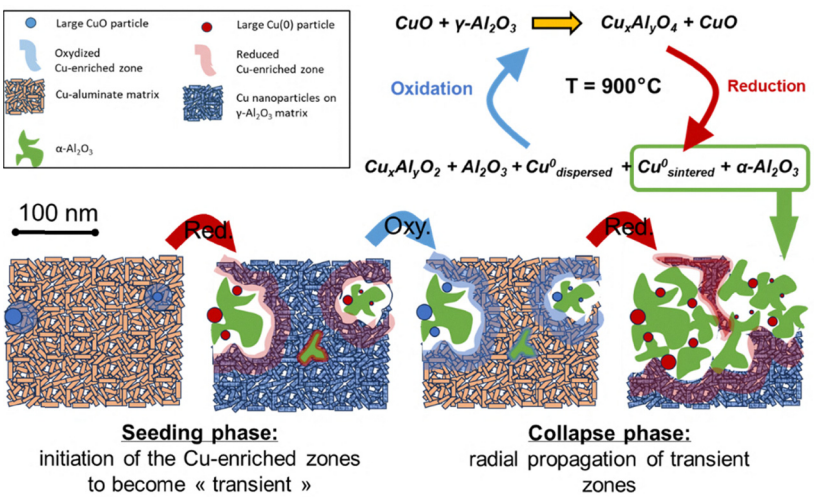

Fig. 9 Conceptual model illustrating the dynamic copper insertion/extraction, formation of Cu-rich zones, and α-Al_2O_3 nucleation as key drivers of irreversible degradation in CuO/Al_2O_3 materials.

performance loss from support restructuring or phase segregation, albeit *via* different mechanisms. CuO/Al_2O_3 remains attractive due to its low reduction temperature and high oxygen transport capacity, but it is especially susceptible to irreversible α-Al_2O_3 formation and Cu sintering. In contrast, Fe-based carriers offer greater thermal stability but slower kinetics, while Mn- and Co-based systems strike a balance between stability and oxygen capacity.

Understanding the interplay between redox environment, support transformation, and metal dispersion—as revealed here for Cu–Al systems—can inform strategies to mitigate degradation in a broader class of oxygen carriers. This includes rational design *via* doping, composite supports, or tailored morphologies to preserve long-term performance under cycling conditions.

Conclusions

In this study, we utilized *in situ* quick XAS (QXAS) to monitor the dynamic structural evolution of CuO/Al_2O_3 materials over 50 oxidation–reduction cycles. This technique captured key phase transitions, revealing a significant decrease in the copper aluminate phase in favor of copper oxide. Our findings indicate a distinct threshold point where a drastic conversion from copper aluminate to copper oxide occurs. By the end of the redox cycles, the material predominantly consisted of α-Al_2O_3 and copper oxide. This transition is closely linked to the growth and propagation of the α-Al_2O_3 phase, suggesting a mechanism driven by particle size effects. Specifically, α-Al_2O_3 formation was initiated after a certain particle size was reached, with subsequent growth occurring through nucleation and growth.

This study demonstrates the strength of QXAS in capturing both second-by-second phase transitions and long-term cycling effects. The MCR-ALS method proved valuable for comprehensive speciation in high-temperature data. SEM complemented QXAS by providing crucial insights into the morphology and texture of the alumina support, addressing the limitations of QXAS by revealing detailed structural information. Together, these techniques offer a robust framework for analyzing complex phase transitions in heterogeneous materials. These insights not only enhance our understanding of the CuO/Al_2O_3 system for chemical looping combustion process but also provide a foundation for investigating other heterogeneous catalytic processes involving intertwined phase interactions across both temporal and spatial dimensions.

Conflicts of interest

There are no conflicts to declare.

Data availability

The data supporting the findings of this study are included in the article and its SI. See DOI: **https://doi.org/10.1039/d5cp00358j**

The raw data generated and analyzed during this study are available from the corresponding author upon reasonable request.

Acknowledgements

The authors are thankful to the Direction of Physics and Analysis at IFP Energies Nouvelles for the SEM characterizations. The work at ROCK was supported by a public grant overseen by the French National Research Agency (ANR) as art of the Investissements d'Avenir program (reference: ANR10-EQPX45). We acknowledge SOLEIL synchrotron facility for providing beamtime under project number 20201423 for access to ROCK beamlines.

References

1 Intergovernmental Panel on Climate Change. Climate Change 2021 The Physical Science Basics; Intergovernmental Panel on Climate Change., 2021.
2 M. Ishida and H. Jin, A Novel Combustor Based on Chemical-Looping Reactions and Its Reaction Kinetics, *J. Chem. Eng. Jpn.*, 1994, **27**(3), 296–301, DOI: **10.1252/jcej.27.296**.
3 A. Lyngfelt, Chemical Looping Combustion: Status and Development Challenges, *Energy Fuels*, 2020, **34**(8), 9077–9093, DOI: **10.1021/acs.energyfuels.0c01454**.
4 Y. De Vos, M. Jacobs, P. Van Der Voort, I. Van Driessche, F. Snijkers and A. Verberckmoes, Development of Stable Oxygen Carrier Materials for Chemical Looping Processes—A Review, *Catalysts*, 2020, **10**(8), 926, DOI: **10.3390/catal10080926**.
5 G. Liu and G. Lisak, Cu-Based Oxygen Carriers for Chemical Looping Processes: Opportunities and Challenges, *Fuel*, 2023, **342**, 127828, DOI: **10.1016/j.fuel.2023.127828**.
6 A. Lambert, A. Tilland, W. Pelletant, S. Bertholin, F. Moreau, I. Clemençon and M. Yazdanpanah, Performance and Degradation Mechanisms of CLC Particles Produced by Industrial Methods, *Fuel*, 2018, **216**, 71–82, DOI: **10.1016/j.fuel.2017.11.115**.
7 M. Pishahang, Y. Larring, R. E. Stensrød, K. A. Andreassen and A. I. Spjelkavik, 3kW Circulating Fluidized Bed Chemical Looping Reactor – A Thermochemical and Chemomechanical Investigation on the Performance of Cu-Impregnated Al_2O_3 as an Oxygen Carrier Material, *Int. J. Greenhouse Gas Control*, 2021, **109**, 103384, DOI: **10.1016/j.ijggc.2021.103384**.
8 M. T. Izquierdo, F. García-Labiano, A. Abad, A. Cabello, P. Gayán, L. F. de Diego and J. Adánez, On the Optimization of Physical and Chemical Stability of a Cu/Al_2O_3 Impregnated Oxygen Carrier for Chemical Looping Combustion, *Fuel Process. Technol.*, 2021, **215**, 106740, DOI: **10.1016/j.fuproc.2021.106740**.
9 A. Cabello, A. Abad, M. T. Izquierdo, P. Gayán, L. F. de Diego, F. García-Labiano and J. Adánez, Qualification of Operating Conditions to Extend Oxygen Carrier Utilization

in the Scaling up of Chemical Looping Processes, *Chem. Eng. J.*, 2022, **430**, 132602, DOI: 10.1016/j.cej.2021.132602.
10 S. Sharna, V. Rouchon, C. Legens, A. Taleb, S. Stanescu, C. Bouillet, A. Lambert, V. Briois, D. Chiche, A. Gay and O. Ersen, Role of Copper Migration in Nanoscale Ageing of Supported CuO/Al_2 O_3 in Redox Conditions: A Combined Multi-scale X-ray and Electron Microscopy Study, *ChemCatChem*, 2023, **15**(4), e202201259, DOI: 10.1002/cctc.202201259.
11 M. Nachtegaal and R. Frahm, *Quick EXAFS Studies in Catalysis*, 2022, pp. 1053–1058, DOI: 10.1107/S1574870720004826.
12 V. Girard, D. Chiche, A. Baudot, D. Bazer-Bachi, L. Lemaitre, V. Moizan-Baslé, A. Rochet, V. Briois and C. Geantet, *In Situ* QXAS Study of Sulfidation/Oxidative Regeneration Reactions of Zinc Molybdate ($ZnMoO_4$) and ZnO–MoO_3 Materials, *Phys. Chem. Chem. Phys.*, 2019, **21**(16), 8569–8579, DOI: 10.1039/C9CP01008D.
13 Q. Imtiaz, P. M. Abdala, A. M. Kierzkowska, W. Van Beek, S. Schweiger, J. L. M. Rupp and C. R. Müller, Na^+ Doping Induced Changes in the Reduction and Charge Transport Characteristics of Al_2O_3-Stabilized, CuO-Based Materials for CO_2 Capture, *Phys. Chem. Chem. Phys.*, 2016, **18**(17), 12278–12288, DOI: 10.1039/C6CP00257A.
14 K. T. Jacob and C. B. Alcock, Thermodynamics of $CuAlO_2$ and $CuAl_2$ O_4 and Phase Equilibria in the System Cu_2O–CuO–Al_2O_3, *J. Am. Ceram. Soc.*, 1975, **58**(5–6), 192–195, DOI: 10.1111/j.1151-2916.1975.tb11441.x.
15 C. Lesage, E. Devers, C. Legens, G. Fernandes, O. Roudenko and V. Briois, High Pressure Cell for Edge Jumping X-Ray Absorption Spectroscopy: Applications to Industrial Liquid Sulfidation of Hydrotreatment Catalysts, *Catal. Today*, 2019, **336**, 63–73, DOI: 10.1016/j.cattod.2019.01.081.
16 J. Jaumot, A. De Juan and R. Tauler, MCR-ALS GUI 2.0: New Features and Applications, *Chemom. Intell. Lab. Syst.*, 2015, **140**, 1–12, DOI: 10.1016/j.chemolab.2014.10.003.
17 J. Jaumot, R. Gargallo, A. De Juan and R. Tauler, A Graphical User-Friendly Interface for MCR-ALS: A New Tool for Multivariate Curve Resolution in MATLAB, *Chemom. Intell. Lab. Syst.*, 2005, **76**(1), 101–110, DOI: 10.1016/j.chemolab.2004.12.007.
18 W. H. Cassinelli, L. Martins, A. R. Passos, S. H. Pulcinelli, C. V. Santilli, A. Rochet and V. Briois, Multivariate Curve Resolution Analysis Applied to Time-Resolved Synchrotron X-Ray Absorption Spectroscopy Monitoring of the Activation of Copper Alumina Catalyst, *Catal. Today*, 2014, **229**, 114–122, DOI: 10.1016/j.cattod.2013.10.077.
19 M. Arjmand, A.-M. Azad, H. Leion, T. Mattisson and A. Lyngfelt, Evaluation of $CuAl_2$ O_4 as an Oxygen Carrier in Chemical-Looping Combustion, *Ind. Eng. Chem. Res.*, 2012, **51**(43), 13924–13934, DOI: 10.1021/ie300427w.
20 J. A. Rodriguez, J. Y. Kim, J. C. Hanson, M. Pérez and A. I. Frenkel, Reduction of CuO in H_2: *In Situ* Time-Resolved XRD Studies, *Catal. Lett.*, 2003, **85**(3/4), 247–254, DOI: 10.1023/A:1022110200942.
21 T. Narushima, H. Tsukamoto and T. Yonezawa, High Temperature Oxidation Event of Gelatin Nanoskin-Coated Copper Fine Particles Observed by *in Situ* TEM, *AIP Adv.*, 2012, **2**(4), 042113, DOI: 10.1063/1.4759498.
22 W. Hu, F. Donat, S. A. Scott and J. S. Dennis, The Interaction between CuO and Al_2O_3 and the Reactivity of Copper Aluminates below 1000 °C and Their Implication on the Use of the Cu–Al–O System for Oxygen Storage and Production, *RSC Adv.*, 2016, **6**(114), 113016, DOI: 10.1039/C6RA22712K.
23 A. M. Volodin, A. F. Bedilo, V. O. Stoyanovskii, V. I. Zaikovskii, R. M. Kenzhin, I. V. Mishakov and A. A. Vedyagin, Nanocrystalline Carbon Coated Alumina with Enhanced Phase Stability at High Temperatures, *RSC Adv.*, 2017, **7**(86), 54852–54860, DOI: 10.1039/C7RA08841H.
24 A. P. Amrute, Z. Łodziana, C. Mondelli, F. Krumeich and J. Pérez-Ramírez, Solid-State Chemistry of Cuprous Delafossites: Synthesis and Stability Aspects, *Chem. Mater.*, 2013, **25**(21), 4423–4435, DOI: 10.1021/cm402902m.
25 I. Levin and D. Brandon, Metastable Alumina Polymorphs: Crystal Structures and Transition Sequences, *J. Am. Ceram. Soc.*, 2005, **81**(8), 1995–2012, DOI: 10.1111/j.1151-2916.1998.tb02581.x.
26 R. B. Bagwell, G. L. Messing and P. R. Howell, The Formation of α-Al_2O_3 from θ-Al_2O_3: The Relevance of a "Critical Size" and: Diffusional Nucleation or "Synchro-Shear"?, *J. Mater. Sci.*, 2001, **36**(7), 1833–1841, DOI: 10.1023/A:1017545213590.
27 S. Lamouri, M. Hamidouche, N. Bouaouadja, H. Belhouchet, V. Garnier, G. Fantozzi and J. F. Trelkat, Control of the γ-Alumina to α-Alumina Phase Transformation for an Optimized Alumina Densification, *Bol. Soc. Esp. Ceram. Vidrio*, 2017, **56**(2), 47–54, DOI: 10.1016/j.bsecv.2016.10.001.
28 N. Sudheer, S. Sharna, V. Rouchon, D. Ihiawakrim, M. Lenertz, P. Levitz, P. Rabu and O. Ersen, Evolution of Correlated Morphological and Structural Disorder in Boehmite-Derived Alumina with Progressive Calcination, *ChemCatChem*, 2024, **16**(20), e202400677, DOI: 10.1002/cctc.202400677.
29 M. Ozawa, Solid-State Thermal Behavior of Copper-Modified Alumina toward Lean-Burn Exhaust NO Removal Catalyst, *Appl. Catal., B*, 1996, **8**(2), 123–140, DOI: 10.1016/0926-3373(95)00061-5.
30 L. M. Plyasova, T. M. Yur'eva, I. Yu Molina, T. A. Kriger, A. M. Balagurov, L. P. Davydova, V. I. Zaikovskii, G. N. Kustova, V. V. Malakhov and L. S. Dovlitova, Dynamics of Structural Transformations in the Reduction of Copper Aluminate, *Kinet. Catal.*, 2000, **41**(3), 429–436, DOI: 10.1007/BF02755383.